Optical interferometer using two-mode squeezed light for enhanced chip-integrated quantum metrology

Patrick Tritschler [1,2,*] Torsten Ohms [1] André Zimmermann [2,3] Fabian Zschocke [4]
Thomas Strohm [4] and Peter Degenfeld-Schonburg [4]

[1]*Bosch Sensortec GmbH, Gerhard-Kindler Straße 9, 72770 Reutlingen, Germany*
[2]*Institute for Micro Integration (IFM), University of Stuttgart, Allmandring 9b, 70569 Stuttgart, Germany*
[3]*Hahn-Schickard, Allmandring 9b, 70569 Stuttgart, Germany*
[4]*Robert Bosch GmbH, Robert-Bosch-Campus 1, 71272 Renningen, Germany*

This paper discusses the possibility of using two-mode squeezed light to improve the performance of existing sensor technology with the focus on its miniaturization under realistic losses. Therefore, we analyze a system consisting of a part for two-mode squeezed light generation, a sensor region, and a detection stage. Based on a general four-wave mixing (FWM) Hamiltonian caused by third-order susceptibility, we formulate linearized equations that describe the FWM process below the threshold and are used to analyze the squeezing quality of the generated optical signal and idler modes. For a possible realization, the focus is set on chip-integrated generation using microring resonators. To do so, the impacts of the design and the pump light are considered in the derived equations. These equations are used to analyze the usage of two-mode squeezed light in quantum metrology and the application in a Mach-Zehnder interferometer. Due to the impact of losses in realistic use cases, we show that the main usage is for small and compact devices, which can lead to a quantum improvement of up to a factor of 10 in comparison with using coherent light only. This enables the use of small squeezing-enhanced sensors with a performance comparable to larger classical sensors.

I. INTRODUCTION

Quantum metrology has the potential to use completely new sensing principles, to enable new use cases, and to increase the sensitivity of existing measurement technology [1]. The main motivation for quantum metrology in comparison to its classical counterpart is that quantum sensors can theoretically overcome the shot-noise limit (SNL) with $1/\sqrt{N}$ and achieve the Heisenberg limit with $1/N$ where N denotes the number of probes, which can be for example the number of photons or the number of measurement repetitions [2,3]. However, in reality this is very challenging to achieve. The reason is that quantum states like single photons are heavily affected by losses and decoherence effects, which makes it difficult to build a Heisenberg-limited quantum sensor [4,5]. Despite this, there are applications which make use of quantum enhancement, like the famous example of gravitational-wave detection. Thereby, single-mode squeezed light is used to increase the phase sensitivity of a huge interferometer to detect extremely small signals caused by gravitational waves [6,7].

In this paper, we show the potential of using two-mode squeezed light generated by four-wave mixing (FWM) for enhanced optical interferometry. The FWM process is utilized in many applications like the creation of frequency combs for sensing and communication [8,9] or squeezed state generation for optical quantum computing [10]. We want to use it to generate two-mode squeezed light for sensing applications. The main focus is on a realistic quantum metrology platform that is realizable with existing technology in photonic integrated circuits.

We see a big potential of quantum metrology for the miniaturization of existing sensor concepts and to realize them in chip-integrated applications. Therefore, we show theoretical derivations of realistic sensor performance, which include the equations required to perform a proper design with typical losses and manufacturing technologies.

The paper is structured as follows. First, the system of interest is discussed in Sec. II, which consists of the state preparation for generating a signal and an idler mode via FWM, a Mach-Zehnder interferometer (MZI) as a sensor region, and a detection stage. Afterwards, each part of the system is discussed in detail. In Sec. III, we start with the discussion of the FWM process in a ring resonator and proceed with the interaction of the environment in Sec. IV to determine the output modes in Sec. V using input-output theory. Subsequently, Sec. VI discusses how the generated modes are used to detect a phase shift (PS) in a lossy MZI. The main results are shown in Sec. VII, in which it is discussed that the combination of squeezed and coherent light can lead to quantum enhancement and that the sensor performance can be improved by an order of magnitude. However, due to optical losses, squeezed light is only useful for a compact or low-loss sensor concept, which leads to an advantage as a two-mode squeezed chip-integrated optical MZI.

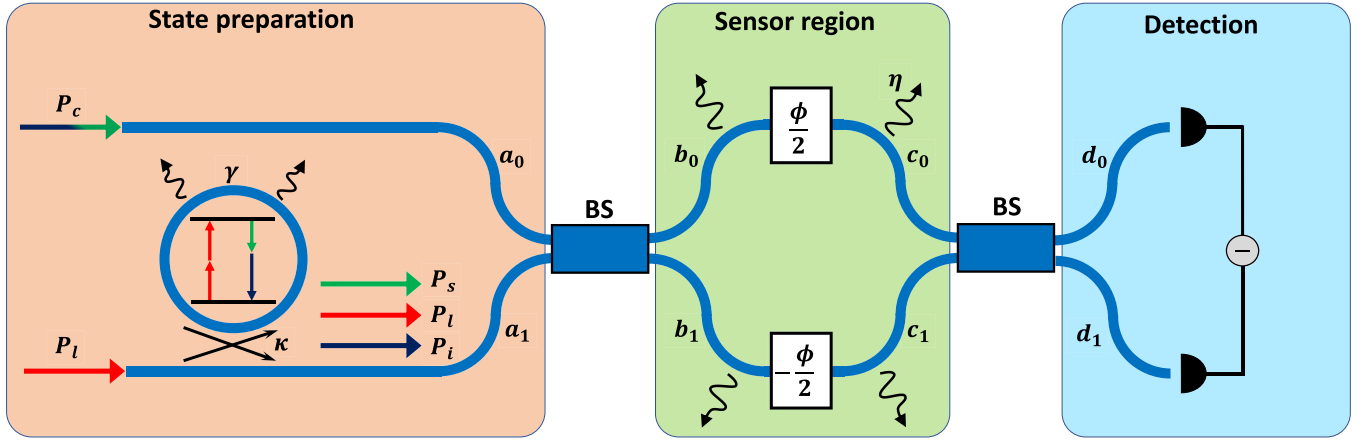*Contact author: patrick.tritschler@bosch-sensortec.com

FIG. 1. Schematic of a MZI which consists of a state preparation (on the left, orange), sensor region (in the middle, green), and detection stage (on the right, blue).

II. SYSTEM OVERVIEW

The system of interest is shown in Fig. 1 and corresponds to an MZI that is pumped by two-mode squeezed and coherent light. It consists overall of three stages with the state preparation, the sensor region, and the detection stage. In the state preparation stage, the system has two inputs in which two coherent light sources can be inserted which are denoted by their power P_l and P_c. While P_c is sent directly to the MZI and corresponds to the input mode a_0, P_l is used to pump a resonator to generate squeezed signal and idle pairs with powers P_s and P_i corresponding to the other input mode of the MZI a_1. Thereby, P_l consists of light with the frequency ω_l and the generated signal and idler light of ω_s and ω_i with $\omega_s + \omega_i = 2\omega_l$.

The resonator is a ring-shaped waveguide that is connected to the straight waveguide and forms a cavity. The light can couple from the straight waveguide into the ring and the other way around by evanescent coupling which can be described by the coupling rate κ. Losses appear inside of the resonator which are described by the loss rate γ. The physical relations to the parameters κ and γ as a function of the design variations of the ring are explained in more detail in Appendix B. Both input modes a_0 and a_1 are mixed at a multimode interferometer which acts as a beam splitter (BS) and are sent into the sensor region of the MZI. For a useful interaction between P_s, P_i, and P_c, it is required that P_c consists of the same frequency components as P_s and P_i with ω_s and ω_i. This is denoted by the colors (gray scales) of each in Fig. 1. Thus, the transmitted power P_l is not required anymore and is filtered out in the following. In this second stage, the light is affected by losses η as well as a phase shift Φ which should be detected and is assumed to be equally distributed between the two light paths. At the end of the sensor region, c_0 and c_1 are mixed at a BS and finally detected at the detection stage using intensity difference detection.

In the following, we first describe the FWM process inside of the resonator and determine the expectation values of the signal and idler modes that form the mode a_1. Afterwards,

we use these results to determine the minimum detectable phase change of the system.

III. FOUR-WAVE MIXING

FWM is a well-known nonlinear optical process which describes the effect of two pump modes $a_p(t)$ being absorbed by a material with a significant third-order susceptibility coefficient $\chi^{(3)}$ while emitting two new modes which are called signal $a_s(t)$ and idler $a_i(t)$ with energy conservation $\omega_i + \omega_s = 2\omega_p$. For simplicity we write a_i for the time dependent operator. Following [11], the Hamiltonian describing FWM inside a cavity is given in the rotating-wave approximation by

$$H_{\text{FWM}} = \hbar\omega_p a_p^\dagger a_p + \hbar\omega_s a_s^\dagger a_s + \hbar\omega_i a_i^\dagger a_i$$
$$+ i\hbar g(a_p a_p a_s^\dagger a_i^\dagger - a_p^\dagger a_p^\dagger a_s a_i) \tag{1}$$

with the nonlinear gain g, which is directly proportional to $\chi^{(3)}$ and is discussed further in Appendix A. The first line of Eq. (1) corresponds to the relevant resonance frequencies in the resonator ω_p, ω_s, and ω_i. The desired FWM process is represented in the second line and denotes the nonlinear interaction in which two pump modes are either absorbed or generated in exchange with one signal and idler mode. In practice, effects such as self-phase modulation and cross-phase modulation also occur, where a mode influences its own and the resonant frequencies of other modes. However, both are neglected in this paper.

A linearization of the FWM part in the Hamiltonian is then performed, assuming the pump mode inside of the resonator to be in a coherent state with the complex amplitude $\langle a_p \rangle = \alpha_p$, which leads to the following Hamiltonian:

$$H_{\text{FWM,lin}} = \hbar(\omega_p \alpha_p^* \alpha_p + \omega_s a_s^\dagger a_s + \omega_i a_i^\dagger a_i)$$
$$+ \frac{i\hbar}{2}(\sigma a_s^\dagger a_i^\dagger - \sigma^* a_s a_i) \tag{2}$$

where $\sigma = 2g\alpha_p^2$ is the injection parameter. Note that the conservation of energy must be fulfilled in the FWM process, but
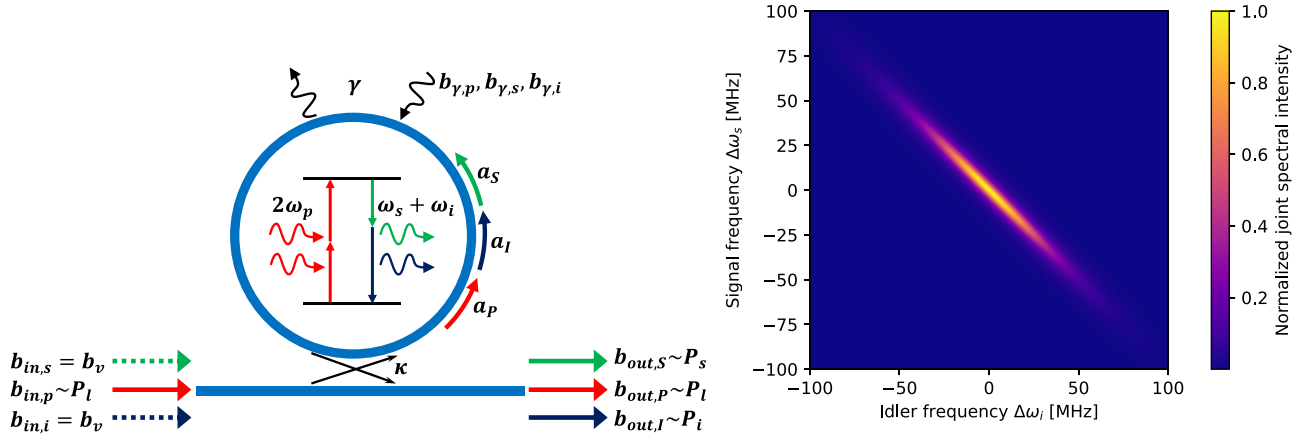
FIG. 2. Left: Ring resonator which is used to generate squeezed light via FWM. A pump mode with the power P_p is coupled via the parameter κ into the cavity, in which a strong pump field generates a signal and idler mode, which couple out of the cavity. Occurring losses inside of the resonator are considered with γ. Right: Joint spectral intensity between the signal and idler mode calculated using Eq. (26) with $X = 0.01$, $n_{\text{eff}} = 1.801$, $n_g = 2.100\,87$, $\alpha_{\text{loss}} = 0.23$ m^{-1}, $L = 2\pi \times 220 \times 10^{-6}$ m, $\omega_p = 1550 \times 10^{-6}$ m, $n_2 = 2.4 \times 10^{-19}$ m^2/W, $A_{\text{eff}} = 1.055\,64 \times 10^{-12}$ m^2, and $\sigma = 0.995\sigma_{\text{th}}$ and normalized by the maximum value of 2.98×10^9.

this is not always the case due to dispersion. To include this effect similarly to [11], the injection parameter can include a FWM detuning $\Delta_\sigma = \omega_s + \omega_i - 2\omega_p$ and a certain phase with

$$\sigma = |\sigma| e^{-i(\Delta_\sigma t - \phi_\sigma)}. \tag{3}$$

This detuning should be zero for the best performance and can be achieved by dispersion engineering of the waveguide geometry [12].

IV. DISSIPATION

To analyze the behavior of FWM inside of a realistic system, it is important to determine the equations of motion of the modes inside of the resonator under the influence of losses and a drive. Therefore, we focus on the desired resonator structure that is shown in Fig. 2. A laser pump mode with the amplitude $\alpha_l = |\alpha_l| \exp(i\phi_l) = \sqrt{P_l/\hbar\omega_l} \exp(i\phi_l)$ and the laser power P_l and phase ϕ_l is coupled from the straight waveguide to the resonator over κ. An enhanced cavity pump field α_p is achieved if the resonance condition is fulfilled with $\omega_r = 2\pi mc/n_{\text{eff}}L$ and the mode index $m = 1, 2, \ldots$, the effective index n_{eff}, and the resonator length L [13]. In the following we assume that this is fulfilled with $\omega_l = \omega_p$. Since we focus on a microscopic device, the integrated resonator is the preferred structure. The advantage is that, due to the field enhancement and the small mode volume, less laser power P_l is required to achieve FWM and to generate squeezed signal and idler modes.

Due to imperfections of the waveguide and mostly caused by scattering, cavity energy is lost which is described by the loss rate γ. Both rates κ and γ describe the photons leaving or entering the cavity due to the respective effect. To include the losses in the equations, it is important to describe the interaction of the ring resonator system with the environment which consists of the straight waveguide and the bath around the ring resonator. From the straight waveguide, the input modes $b_{\text{in},s}$, $b_{\text{in},i}$ and $b_{\text{in},p}$ couple from the waveguide in the ring, while the resonator modes couple from the ring into the waveguide. The bath modes $b_{\gamma,s}$, $b_{\gamma,i}$, and $b_{\gamma,p}$ interact through the losses γ with the resonator modes. Thereby, we

assume the waveguide modes $b_{\text{in},s}$ and $b_{\text{in},i}$ and the bath modes to be in the vacuum state, while $b_{\text{in},p}$ represents the coherent pump α_p. In Appendix D, we also discuss the case of a coherent part in $b_{\text{in},s}$ and $b_{\text{in},i}$.

It is well known that the interaction between the system and the environment can be described in dependency of the decay rates with $\sqrt{\kappa}b_{\text{in},\mu}$ and $\sqrt{\gamma}b_{\gamma,\mu}$ and the modes $\mu = p, s, i$ [14–16]. This leads to the following interaction Hamiltonian in the rotating-wave approximation:

$$H_{\text{int}} \approx i\hbar \left(\sqrt{\frac{\kappa}{2\pi}} \int_{-\infty}^{\infty} d\omega \sum_{\mu=i,s,p} [a_\mu b_{\text{in},\mu}^\dagger(\omega) - a_\mu^\dagger b_{\text{in},\mu}(\omega)] \right.$$
$$\left. + \sqrt{\frac{\gamma}{2\pi}} \int_{-\infty}^{\infty} d\omega \sum_{\mu=i,s,p} [a_\mu b_{\gamma,\mu}^\dagger(\omega) - a_\mu^\dagger b_{\gamma,\mu}(\omega)] \right). \tag{4}$$

Note that if the wavelength difference for the signal, idler, and pump is significant it is important to distinguish between the coupling and loss rates of each. Both rates would then require the corresponding indices.

With Eqs. (2) and (4), it is possible to derive the quantum Langevin equation of motion in the Heisenberg picture describing the intracavity modes in dependency of the bath and waveguide modes which can be derived for our system using [15,17]

$$\frac{da_\mu(t)}{dt} = -\frac{i}{\hbar}[a_\mu(t), H_{\text{FWM,lin}}]$$
$$- \frac{\gamma + \kappa}{2} a_\mu(t) + \sqrt{\kappa} b_{\text{in},\mu}(t) + \sqrt{\gamma} b_{\gamma,\mu}(t). \tag{5}$$

Thereby, the modes $b_{\text{in},\mu}(t)$ and $b_{\gamma,\mu}(t)$ of Eq. (5) are in units of $\sqrt{\text{Hz}}$ and are connected by a Fourier transformation with the corresponding modes of Eq. (4). This is explicitly denoted by the dependency of either t or ω. First, we solve Eq. (5) for the pump mode. The fluctuations in the pump mode can be neglected in this case due to the strong coherent background. Setting $\langle a_p \rangle = \alpha_p$, this leads to the following equation of

motion:

$$\frac{d}{dt}\alpha_p(t) = -i\omega_p\alpha_p(t) - \frac{\gamma+\kappa}{2}\alpha_p(t) + \sqrt{\kappa}\alpha_l(t). \quad (6)$$

This equation is solved by performing a Fourier transformation, which leads to

$$\alpha_p(\omega) = \frac{\sqrt{\kappa}\alpha_l(\omega)}{(\gamma+\kappa)/2 - i(\omega-\omega_p)} \quad (7)$$

with the detuning from the resonance wavelength $\Delta_p = \omega - \omega_p$, which is an important part if effects like self-phase modulation or optical bistability are considered. Note that while α_l has the units of $\sqrt{\text{Hz}}$, the intracavity mode α_p is unitless. The reason is that while the modes outside of the resonator correspond to a photon flux in units of $\sqrt{\text{Hz}}$ the mode α_p describes the field of the resonator over the whole mode volume. It is described in Appendix B how to transfer α_p back to a physical unit which corresponds to a photon flux. For the intracavity signal and idler modes, the fluctuations are relevant and the equation of motion can be given as

$$\frac{da_{s/i}(t)}{dt} = -i\omega_{s/i}a_{s/i}(t) + \frac{\sigma}{2}a^\dagger_{i/s}(t) - \frac{\gamma}{2}a_{s/i}(t) - \frac{\kappa}{2}a_{s/i}(t)$$
$$+ \sqrt{\kappa}b_{\text{in},s/i}(t) + \sqrt{\gamma}b_{\gamma,s/i}(t). \quad (8)$$

V. INPUT-OUTPUT THEORY

To be able to determine the performance of sensor systems using the generated two-mode squeezed states, it is required to solve the equations of motions (8) and to determine the expectation values of the output modes that depend on the geometrical and pump parameters. In the following, we derive and validate the equations and analyze the squeezing of the output modes.

A. Linearized outracavity equations

To derive the output modes b_{out} of Fig. 2, we use the boundary condition that has already been derived in [14,15] and that has been proven to be valid for vacuum and coherent input modes with

$$b_{\text{in},s/i}(t) = \sqrt{\kappa}a_{s/i}(t) - b_{\text{out},s/i}(t). \quad (9)$$

Thereby, $b_{\text{out},s/i}$ correspond to the signal and idler output modes, which couple from the ring to the straight waveguide and have the same units as $b_{\text{in},s/i}$ with $\sqrt{\text{Hz}}$. This leads to the following equations of motion describing the intracavity field using the output operator:

$$\frac{da_{s/i}(t)}{dt} = -i\omega_{s/i}a_{s/i}(t) + \frac{\sigma}{2}a^\dagger_{i/s}(t) - \frac{\gamma}{2}a_{s/i}(t) + \frac{\kappa}{2}a_{s/i}(t)$$
$$- \sqrt{\kappa}b_{\text{out},s/i}(t) + \sqrt{\gamma}b_{\gamma,s/i}(t). \quad (10)$$

For a more compact description, Eqs. (8) and (10) can be given in matrix notation as follows for the input and output operators:

$$\frac{d}{dt}\mathbf{A}(t) = \left(\mathbf{K} + \frac{\kappa}{2}\mathbb{1}\right)\mathbf{A}(t) + \sqrt{\kappa}\mathbf{B}_{\text{in}}(t) + \sqrt{\gamma}\mathbf{B}_\gamma(t), \quad (11)$$

$$\frac{d}{dt}\mathbf{A}(t) = \left(\mathbf{K} - \frac{\kappa}{2}\mathbb{1}\right)\mathbf{A}(t) - \sqrt{\kappa}\mathbf{B}_{\text{out}}(t) + \sqrt{\gamma}\mathbf{B}_\gamma(t). \quad (12)$$

Thereby, $\mathbb{1}$ is the 4×4 identity matrix and we use the following notations for the other matrices:

$$\mathbf{B}_{\text{in}} = \begin{pmatrix} b_{\text{in},s} \\ b^\dagger_{\text{in},s} \\ b_{\text{in},i} \\ b^\dagger_{\text{in},i} \end{pmatrix}, \quad \mathbf{B}_\gamma = \begin{pmatrix} b_{\gamma,s,} \\ b^\dagger_{\gamma,s} \\ b_{\gamma,i} \\ b^\dagger_{\gamma,i} \end{pmatrix}, \quad (13)$$

$$\mathbf{A} = \begin{pmatrix} a_s \\ a^\dagger_s \\ a_i \\ a^\dagger_i \end{pmatrix}, \quad \mathbf{B}_{\text{out}} = \begin{pmatrix} b_{\text{out},s} \\ b^\dagger_{\text{out},s} \\ b_{\text{out},i} \\ b^\dagger_{\text{out},i} \end{pmatrix}, \quad (14)$$

$$\mathbf{K} = \begin{pmatrix} -i\omega_s - \frac{\gamma}{2} & 0 & 0 & \frac{\sigma}{2} \\ 0 & i\omega_s - \frac{\gamma}{2} & \frac{\sigma^*}{2} & 0 \\ 0 & \frac{\sigma}{2} & -i\omega_i - \frac{\gamma}{2} & 0 \\ \frac{\sigma^*}{2} & 0 & 0 & i\omega_i - \frac{\gamma}{2} \end{pmatrix}. \quad (15)$$

Performing a Fourier transformation on Eqs. (11) and (12) leads to the following matrix notations of the equation of motion in the frequency domain:

$$\left[\mathbf{\Omega} - \mathbf{K} + \frac{\kappa}{2}\mathbf{I_4}\right]\mathbf{A}(\omega) = \sqrt{\kappa}\mathbf{B}_{\text{in}}(\omega) + \sqrt{\gamma}\mathbf{B}_\gamma(\omega), \quad (16)$$

$$\left[\mathbf{\Omega} - \mathbf{K} - \frac{\kappa}{2}\mathbf{I_4}\right]\mathbf{A}(\omega) = -\sqrt{\kappa}\mathbf{B}_{\text{out}}(\omega) + \sqrt{\gamma}\mathbf{B}_\gamma(\omega), \quad (17)$$

where $\mathbf{\Omega}$ is the frequency matrix with

$$\mathbf{\Omega} = \begin{pmatrix} -i\omega & 0 & 0 & 0 \\ 0 & i\omega & 0 & 0 \\ 0 & 0 & -i\omega & 0 \\ 0 & 0 & 0 & i\omega \end{pmatrix}. \quad (18)$$

This is now a linear equation system which can be re-arranged to eliminate the intracavity modes and to determine the output modes of the system using only the bath modes, waveguide modes, and system operators with

$$\mathbf{B}_{\text{out}}(\omega) = -\frac{1}{\sqrt{\kappa}}\left[\left[\mathbf{\Omega} - \mathbf{K} - \frac{\kappa}{2}\mathbf{I_4}\right]\left[\mathbf{\Omega} - \mathbf{K} + \frac{\kappa}{2}\mathbf{I_4}\right]^{-1}\right.$$
$$\left.[\sqrt{\kappa}\mathbf{B}_{\text{in}}(\omega) + \sqrt{\gamma}\mathbf{B}_\gamma(\omega)] - \sqrt{\gamma}\mathbf{B}_\gamma(\omega)\right]. \quad (19)$$

Note that by subtracting $\mathbf{\Omega}$ from $\mathbf{K}$ we introduce the detunings of the signal and idler mode with $\Delta_i = \omega - \omega_i$ and $\Delta_s = \omega - \omega_s$, which are zero for a perfect cavity design and FWM phase matching.

By using Eq. (19), it is possible to determine the expectation values of the output modes. To achieve this, we make use of the canonical commutation relations of the vacuum modes b_v, which leads to the following expectation values [18,19]:

$$\langle b_v(t)\rangle = \langle b^\dagger_v(t)\rangle = \langle b_v(t)b_v(t')\rangle = \langle b^\dagger_v(t)b_v(t')\rangle = 0$$

$$\langle b_v(t)b^\dagger_v(t')\rangle = \delta(t-t'). \quad (20)$$

While the results for all expectation values are given in Appendix D, we want to give particular emphasis to the
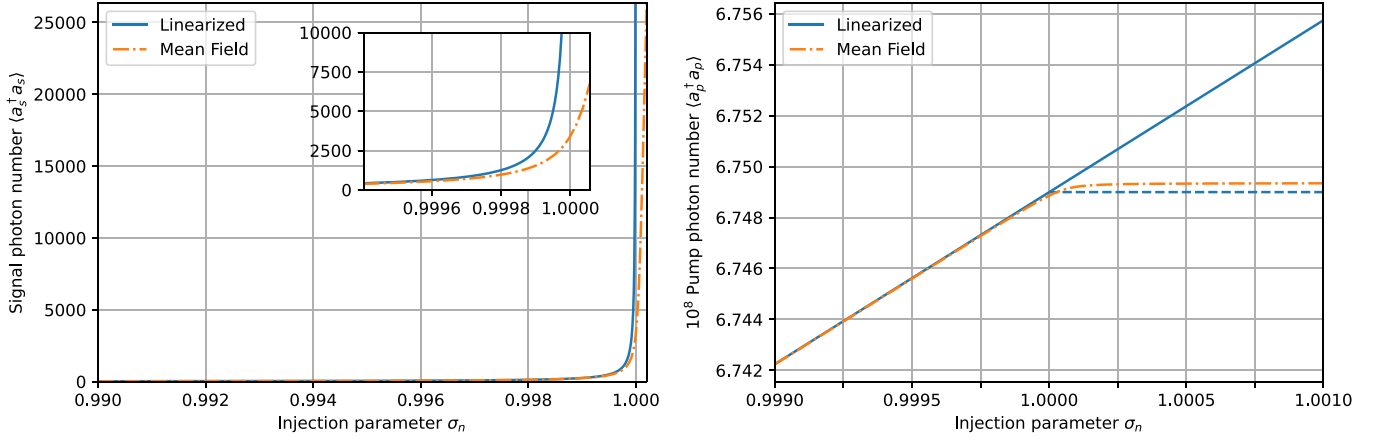
FIG. 3. Left: Signal photon number $\langle a_p^\dagger a_p \rangle$ for the linearized approach (solid blue) and MF (dashed dotted orange). Right: Pump photon number $\langle a_p^\dagger a_p \rangle$ for the linearized approach (solid blue), the solution of the linearized approach at the threshold (dashed blue), and MF (dashed dotted orange). For both the following values are used: $\Delta_i = \Delta_s = \Delta_p = 0$, $X = 0.01$, $n_{\text{eff}} = 1.801$, $n_g = 2.100\,87$, $\alpha_{\text{loss}} = 0.23$ m^{-1}, $L = 2\pi \times 220 \times 10^{-6}$ m, $\lambda_p = 1550 \times 10^{-6}$ m, $n_2 = 2.4 \times 10^{-19}$ m^2/W, $A_{\text{eff}} = 1.055\,64 \times 10^{-12}$ m^2.

expectation value of the output signal photon number, which is

$$\langle b_{\text{out},s}^\dagger(\omega) b_{\text{out},s}(\omega') \rangle = \frac{4\sigma^2 \kappa \Gamma}{\Xi - 2\sigma^2 \Gamma^2} \delta(\omega - \omega')$$

$$\stackrel{\Delta_i = \Delta_s = 0}{=} \frac{4\sigma^2 \kappa \Gamma}{(\Gamma^2 - \sigma^2)^2} \delta(\omega - \omega') \qquad (21)$$

with

$$\Xi = (4\Delta_i \Delta_s - \sigma^2)^2 + 4\Gamma^2(\Delta_i^2 + \Delta_s^2) + \Gamma^4 \qquad (22)$$

and the total losses of the cavity modes $\Gamma = \gamma + \kappa$. It is important to note that Eq. (21) diverges for $\sigma = \Gamma := \sigma_{\text{th}}$, which corresponds to the threshold of the FWM process and is discussed in more detail in Appendix B.

B. Mean-field theory

The divergence in Eq. (21) is not physical and, thus, it is necessary to know the range of σ in which the derived equations are valid as well as to validate the linearized Hamiltonian approach. For this, the results of the expectation values are determined using the mean-field (MF) theory. Therefore, we use the drive term

$$H_{\text{d}} = i\hbar(\sqrt{\kappa} \alpha_l a_p^\dagger - \sqrt{\kappa} \alpha_l^* a_p) \qquad (23)$$

as well as the FWM Hamiltonian from Eq. (1) and the linearized one in Eq. (2) to derive a master equation describing the intracavity modes for the MF as well as the linearized approach with

$$\frac{d\rho_{\text{MF}}}{dt} = -\frac{i}{\hbar}[H_{\text{FWM}} + H_{\text{d}}, \rho_{\text{MF}}]$$
$$+ \sum_{j=i,s,p} \Gamma\left[a_j \rho_{\text{MF}} a_j^\dagger - \frac{1}{2}(a_j^\dagger a_j \rho_{\text{MF}} + \rho_{\text{MF}} a_j^\dagger a_j) \right]$$

$$\qquad (24)$$

$$\frac{d\rho_{\text{lin}}}{dt} = -\frac{i}{\hbar}[H_{\text{FWM,lin}}, \rho_{\text{lin}}]$$
$$+ \sum_{j=i,s} \Gamma\left[a_j \rho_{\text{lin}} a_j^\dagger - \frac{1}{2}(a_j^\dagger a_j \rho_{\text{lin}} + \rho_{\text{lin}} a_j^\dagger a_j) \right]. \qquad (25)$$

In comparison to the MF master equation, the pump mode does not appear in the linearized equation. Each of the master equations leads to a coupled equation system which can be solved to determine the expectation values using a numerical approach. However, for the MF approach, nonlinear terms arise which are solved by decoupling the expectation values of the pump mode from the signal and idler modes with for example $\langle a_p^\dagger a_p a_s a_i \rangle = \langle a_p^\dagger a_p \rangle \langle a_s a_i \rangle$. Thus, MF is a more realistic view since the pump mode still appears in the Hamiltonian as an operator. Knowing that MF is not perfect as well, it has been shown that it is very accurate below the threshold [20–22]. Thus, we can use it to validate the range of σ.

Values of a real system are used to perform a simulation of an optical silicon nitride (Si$_3$N$_4$) waveguide with the height of 800 nm, a width of 1.2 μm, and a bend radius of 220 μm using a mode solver at a pump wavelength of $\lambda_p = 1.55$ μm. This dimension is in the range where squeezing generation with a ring resonator has already been demonstrated [23]. The nonlinear index is approximated to be 2.4×10^{-19} m^2/W based on [24] which leads to $g = 1.5$ Hz. Losses of $\alpha_{\text{loss}} = 1$ dB/m and a ring transmission of 0.01 are assumed. This leads to $\gamma = 38.3$ MHz and $\kappa = 1208$ MHz.

The results for the signal photon number $\langle a_s^\dagger a_s \rangle$ and the pump photon number $\langle a_p^\dagger a_p \rangle$ are shown in Fig. 3 as a function of the normalized injection parameter $\sigma_n = \sigma / \sigma_{\text{th}}$ which is exactly 1 at the threshold. While for MF $\langle a_p^\dagger a_p \rangle$ is determined using the master equation, the linearized approach is solved using Eq. (7). It can be seen that pump depletion appears at $\sigma_c = 1$ for MF while $\langle a_p^\dagger a_p \rangle$ rises for the linearized approach. For $\langle a_s^\dagger a_s \rangle$ it can be seen that the linearized approach diverges at $\sigma_n = 1$, while the MF solution is still rising reasonably. The MF and the linearized solution split just before the threshold, which shows that the linearized approach can be used close to the threshold. Tolerating an error of 5%, σ is valid from a value of zero up to $0.998\,95\sigma_{\text{th}}$.

C. Outracavity squeezing

The squeezing of the outracavity modes can be analyzed by using the expectation results determined with the linearized

theory of Eq. (19). It is of special interest for this paper how the two-mode squeezing of the outracavity signal and idler modes behaves depending on the system parameters. One way to analyze the squeezed light is the joint spectral intensity Φ, which depends on the wavelength of the generated signal and idler. It is known from energy conservation of FWM with $2\omega_p = \omega_s + \omega_i$ that if the signal has the detuning δ_ω from ω_p the idler has the distance $-\delta_\omega$. Consequently, this leads to the definitions of the FWM detuning $\Delta_s = \Delta\omega_s$ as well as $\Delta_i = -\Delta\omega_i$. Thereby, $\Delta\omega_s$ is the distance from ω_s and $\Delta\omega_i$ is the distance from ω_i. The joint spectral intensity between the signal and idler results then in the following equation:

$$\Phi(\omega, \omega') = \langle b_{\text{out},s}^\dagger(\omega) b_{\text{out},i}^\dagger(\omega') b_{\text{out},s}(\omega) b_{\text{out},i}(\omega') \rangle$$
$$= \frac{16\kappa^2\sigma^4\Gamma^2 + 4\kappa^2\sigma^2[\Lambda + (\Gamma^2 + \sigma^2)^2]}{[\Lambda + (\Gamma^2 - \sigma^2)^2]^2} \delta(\omega - \omega'),$$

(26)

with $\Lambda = 16\Delta\omega_s^2\Delta\omega_i^2 + 8\Delta\omega_s\Delta\omega_i\sigma^2 + 4\Gamma^2(\Delta\omega_s^2 + \Delta\omega_i^2)$. It can be interpreted as the joint signature probability distribution that indicates the probability to detect a signal photon at a certain frequency if an idler is detected at another frequency. Thus, it is an indication for the correlation between the two modes as a function of the frequency [25]. The result of Φ is shown in Fig. 2 over the signal and idler frequency with the same values for the geometry as above and $\sigma_n = 0.995$. It is interesting that the spectrum is squeezed with a high correlation and broadband in the case of an asymmetric detuning between the signal and the idler. This behavior can be explained by the energy conservation, which must be fulfilled and means that if the signal is generated at a higher frequency compared to the pump frequency the idler must be generated at a lower frequency.

Another important feature of squeezed light is the quadrature operator which allows the analysis of the noise behavior with [26]

$$X_Q(\omega) = \frac{1}{\sqrt{2}}[(b_{\text{out},s}(\omega) + b_{\text{out},i}(\omega))e^{i\phi_{\text{LO}}} + \text{H.c.}]$$ (27)

with the local oscillator (LO) phase ϕ_{LO}. In experiments this phase can be used to change the measured signal from low noise or squeezing at $\phi_{\text{LO}} = \pi/2$ to high noise or antisqueezing at $\phi_{\text{LO}} = 0$. Thereby, the outracavity light is mixed with a coherent local oscillator laser with a certain phase to realize the desired quadrature operator as shown in Fig. 4 and experimentally demonstrated in [23]. This setup is also discussed in detail in Appendix C. Of special interest is the variance of the quadrature to identify the noise of the two-mode squeezed light which is defined as [26]

$$V(\omega, \omega') = \Delta X_Q(\omega, \omega')$$
$$= \langle X_Q(\omega) X_Q(\omega') \rangle - \langle X_Q(\omega) \rangle \langle X_Q(\omega') \rangle$$
$$\xrightarrow{b_{\text{in},s/i}=b_v} \langle X_Q(\omega) X_Q(\omega') \rangle.$$ (28)

For the case of zero detuning, the following equations are determined for the variance in the squeezed and antisqueezed
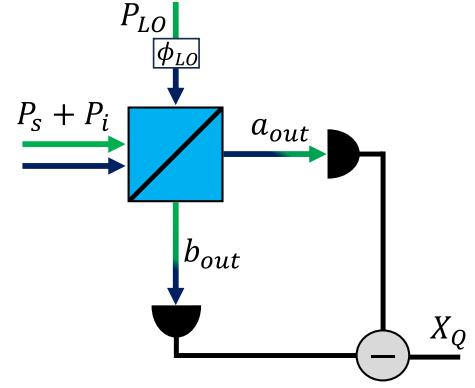

FIG. 4. Homodyne measurement to realize the measurement of the quadrature operator with the local oscillator consisting of a strong coherent background and a certain phase ϕ_{LO} with the same frequencies as P_s and P_i.

case with integrating over ω to remove the δ function, which leads to

$$V_{\phi_{\text{LO}}=\pi/2} = \frac{\Gamma^2 + \sigma^2}{(\Gamma - \sigma)^2} - \frac{2\sigma(\kappa - \gamma)}{(\Gamma - \sigma)^2},$$ (29)

$$V_{\phi_{\text{LO}}=0} = \frac{\Gamma^2 + \sigma^2}{(\Gamma + \sigma)^2} + \frac{2\sigma(\kappa - \gamma)}{(\Gamma + \sigma)^2}.$$ (30)

The results of Eq. (28) over the phase ϕ_{LO} are shown in Fig. 5 with the same geometry values as above. The different colors and line styles represent various values of the pump power σ_n and it can be seen that with rising power the squeezing improves while the antisqueezing increases. A squeezing of approximately -15.02 dB can be achieved for the defined limit $\sigma_n = 0.99895$. This is close to the value with less pump $\sigma_n = 0.95$ with -15.01 dB which is about -12 dB lower than vacuum, and thus good noise reduction can be already achieved with a power close to the threshold. However, the difference for the antisqueezing is significantly larger with 65.46 dB for $\sigma_n = 0.99895$ and 31.68 dB for $\sigma_n = 0.95$.

For the design it is important to know how the ring geometries affect the squeezing. In this case, the two main
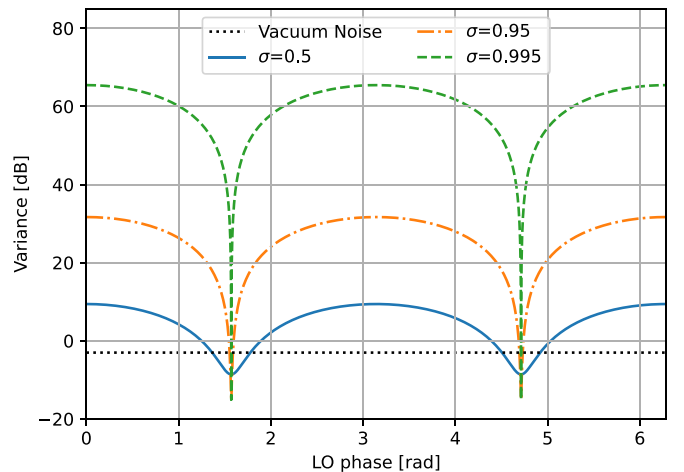

FIG. 5. Variance of the two-mode squeezed light calculated using Eq. (28) over the LO phase with a variation of σ_n.
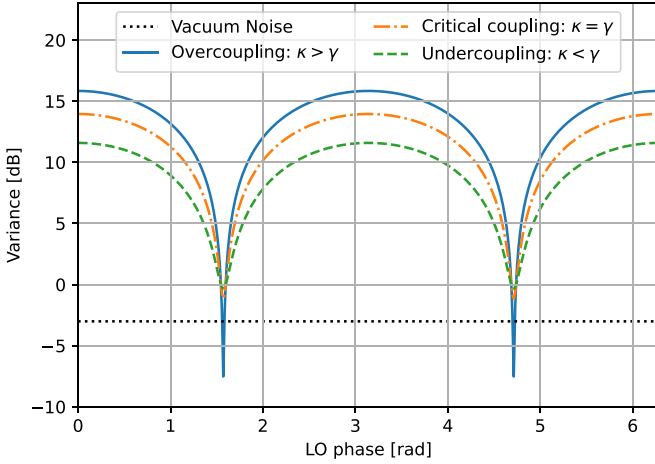
FIG. 6. Variance of the two-mode squeezed light calculated using Eq. (28) over the LO phase with a variation of κ and γ. The variations are achieved with $\alpha_{\text{loss}} = 0.23$ m^{-1} for overcoupling, $\alpha_{\text{loss}} = 7.28$ m^{-1} for critical coupling, and $\alpha_{\text{loss}} = 23.04$ m^{-1} for undercoupling while σ_n is constant at 0.95.

parameters are the decay rates κ and γ which can be tuned by the ring design. The influences for different ratios between κ and γ are shown in Fig. 6. The best squeezing can be achieved for the case $\kappa > \gamma$ which is also known as overcoupling, since more light couples in and out of the ring than is lost due to losses. For the so-called critical coupling case in which both coupling rates are equal with $\kappa = \gamma$, the squeezing decreases and for the undercoupling case with $\kappa < \gamma$ the variance is larger compared to the vacuum noise. It is reasonable that $\kappa > \gamma$ is required for a good squeezing, since only if the squeezed signal and idler pairs couple out of the resonator they contribute to a squeezing. This matches the results of other works and shows the importance of a proper cavity design [27].

Another feature that is often given in the literature to describe squeezed light is the squeezing parameter r. By comparison with results for two-mode squeezed light in the literature [28], we can derive it to

$$
\begin{aligned}
r &= \sinh^{-1}\left(\sqrt{\langle b_{\text{out},s}^\dagger b_{\text{out},s}\rangle}\right) \\
&= \sinh^{-1}\left(\sqrt{\frac{4\sigma^2\kappa\Gamma}{\Xi - 2\sigma^2\Gamma^2}}\right).
\end{aligned}
\tag{31}
$$

Using the same values as for Fig. 5 with $\sigma_n = 0.998\,95$, a squeezing parameter of $r = 7.54$ can be achieved.

VI. MACH-ZEHNDER INTERFEROMETER

The main goal of this paper is to show the potential of two-mode squeezed states generated by FWM in a sensor application that is built in the form of an MZI and to determine the sensing limit. The considered system from Fig. 1 is split into a part for the state preparation, the sensor region, and the detection.

At the state preparation, pump light P_l is sent into the ring resonator for the signal and idler generation, while additional

coherent light P_c is coupled in the other input of the MZI. The generated outracvity signal and idler mode correspond to the state a_1 and P_c corresponds to a_0. They are sent into the MZI via the BS. The states then enter the sensor area, which applies a symmetrical PS to them that is to be measured. The BS and PS can be defined as follows:

$$
\mathbf{BS} = \frac{1}{\sqrt{2}}\begin{pmatrix} 1 & 1 \\ 1 & -1 \end{pmatrix}, \mathbf{PS} = \begin{pmatrix} e^{i\frac{\phi}{2}} & 0 \\ 0 & e^{-i\frac{\phi}{2}} \end{pmatrix}.
\tag{32}
$$

The sensor region is typically the largest area of the system and thus it is important to consider losses to model a realistic application. Therefore, the efficiency η is introduced, which is related to the mode power and is 1 for the lossless case. In chip-integrated applications η depends on the waveguide losses α_{loss} and the length of the sensor region L with

$$
\eta = e^{-\alpha_{\text{loss}}L}.
\tag{33}
$$

The derivation of Eq. (33) is discussed in more detail in Appendix B. To consider the effect of losses, we use a BS that couples with η a vacuum mode b_v into the system while coupling out the system mode [5]. This is discussed in Appendix E. The loss must be applied to each path of the MZI with two uncorrelated vacuum modes $\mathbf{B} = (b_{v,0}\ b_{v,1})^\top$. After the sensor region, another BS follows and the modes at the detection stage $\mathbf{D} = (d_0\ d_1)^\top$ can be determined in dependency of the input modes $\mathbf{A} = (a_0\ a_1)^\top$ with

$$
\mathbf{D} = \mathbf{BS} \cdot [\sqrt{\eta} \cdot \mathbf{PS} \cdot \mathbf{BS} \cdot \mathbf{A} + \sqrt{1-\eta} \cdot \mathbf{B}].
\tag{34}
$$

Afterwards, the output modes are detected and further processed with some electronic circuits. For the detection scheme, we use the commonly used intensity difference detection which is defined as

$$
\mathrm{ID} = d_0^\dagger d_0 - d_1^\dagger d_1.
\tag{35}
$$

It is obvious that in reality losses appear at each stage like at the detector and the electronic processing, which should be modeled using a loss BS [29]. As shown in [5] it is sufficient to focus on the losses within the optical system because these are the most significant ones and the other losses can be merged to this loss.

VII. QUANTUM-SENSING LIMIT

To derive the performance and the quantum enhancement of the system, it is necessary to determine the noise of the measurement operator. In general the minimum detectable phase change inside of the MZI $\Delta\phi$ can be evaluated using error propagation [5,30]:

$$
\Delta\phi = \frac{\sqrt{\Delta\mathrm{ID}}}{|\delta\langle\mathrm{ID}\rangle/\delta\phi|}
\tag{36}
$$

with $\Delta\mathrm{ID} = \langle\mathrm{ID}^2\rangle - \langle\mathrm{ID}\rangle^2$. Therefore, the previously derived expectation values are required. Since higher-order expectation values appear in Eq. (36), we use the helpful cumulant expansion which decreases the order of an operator $\mathbf{X} = \langle X_1 X_2 \ldots X_n\rangle$ [31]:

$$
\langle X_1 X_2 \ldots X_n\rangle = \sum_{p\in P(I)/I} (|p|-1)!(-1)^{|p|}\prod_{B\in p}\left\langle\prod_{i\in B} X_i\right\rangle
\tag{37}
$$

with $I = \{1, 2, \ldots, n\}$, $P(I)/I$ being the set of all operators excluding I, $|p|$ the length of the partition p, and B the block of each partition. An example for $n = 3$ is

$$\langle X_1 X_2 X_3 \rangle = \langle X_1 X_2 \rangle \langle X_3 \rangle + \langle X_1 X_3 \rangle \langle X_2 \rangle$$
$$+ \langle X_1 \rangle \langle X_2 X_3 \rangle - 2 \langle X_1 \rangle \langle X_2 \rangle \langle X_3 \rangle. \quad (38)$$

Using this, it is possible to determine the noise of the measured signal and thus to find out the minimal detectable phase change of the system.

In Appendix F, it is shown that the optimal phase sensitivity in our setting can be achieved for a phase difference of $\phi_{\text{opt}} = \pi/2$ between the two paths of the MZI. Thus, the results in the following are evaluated at this operation point.

If the MZI is operated using only P_c with the mode amplitude α_c and without using P_l for the squeezed light generation, the phase sensitivity using only coherent light in the sensor region $\Delta\phi_{\text{c}}$ is given by the following expression:

$$\Delta\phi_{\text{c}} = \frac{1}{\sqrt{\eta}\alpha_c}. \quad (39)$$

Equation (39) scales as well as the SNL with $1/\alpha_c$ for the lossless case and with losses it is slightly worse. For the case of using P_l to pump the ring resonator to generate squeezed light and mixing this with coherent light P_c, the phase sensitivity using squeezed light $\Delta\phi_{\text{s}}$ at ϕ_{opt} can be expressed as

$$\Delta\phi_{\text{s}} = \frac{\sqrt{\eta\alpha_c^2(\Gamma - \sigma)^2(\Gamma^2 + \sigma(2\gamma - 6\kappa) + \sigma^2) + \alpha_c^2(\Gamma^2 - \sigma^2)^2 + 8\kappa\sigma^2\Gamma}}{\sqrt{\eta}(\Gamma^2 - \sigma^2)\left|\alpha_c^2 - \frac{8\sigma^2\kappa\Gamma}{(\Gamma^2-\sigma^2)^2}\right|}. \quad (40)$$

Two poles can appear. One at $\sigma = \Gamma$, which is however not in the valid range of σ, and the second one if the number of squeezed photons $\langle b_{\text{out},s}^\dagger b_{\text{out},s} \rangle + \langle b_{\text{out},i}^\dagger b_{\text{out},i} \rangle$, given by Eq. (21), matches the number of coherent photons α_c^2. This can be seen in the denominator of Eq. (40). However, this only appears for rather small values of α_c, since the number of squeezed photons is limited in practice. Thus, α_c should be chosen large enough, which in most applications is easy reachable since the number of squeezed photons is small. This behavior is analyzed in more detail in Appendix F.

For the optimal conditions, with no losses and thus with $\eta = 1$, $\gamma = 0$, and a large amount of coherent photons with $\alpha_c > 10^4$, the phase sensitivity of Eq. (40) can be approximated by the following expression:

$$\Delta\phi_{\text{s,opt}} \approx \frac{\sqrt{2}}{\alpha_c} \frac{\kappa - \sigma}{\kappa + \sigma}. \quad (41)$$

Depending on the degree of squeezing described by the values for κ and σ, an improvement in scaling over Eq. (39) and the SNL can be achieved by up to three orders of magnitude within the valid range of σ. However, Eq. (41) is challenging to achieve in a real world application, since losses will appear.

To identify how well both systems perform in a more realistic and lossy setting, it is necessary to also analyze the SNL of the system. This SNL is calculated with the total number of photons inside of the MZI. However, as indicated in the state preparation stage in Fig. 1, the pump power that is required to generate the two-mode squeezed light is included as well in the SNL. This results in the following equation for the SNL:

$$\Delta\phi_{\text{SNL}} = \frac{1}{\sqrt{N}} = \frac{1}{\sqrt{\langle d_0^\dagger d_0 \rangle + \langle d_1^\dagger d_1 \rangle + |\alpha_l|^2}}, \quad (42)$$

with the number of photons in the system N. The addition of α_l is required since the pump is not modeled in the out-racavity expectation values. In our opinion, it is important to include α_l in Eq. (42). The reason is that α_l is used inside the sensor system to pump the ring resonator and to generate the squeezed light and thus it already takes part in the whole sensor performance. Pumping the ring resonator only makes

sense if the generation of squeezed light is more advantageous than using the pump power directly for the phase detection in the sensor region. This fact can be made more comparable if α_l is included in Eq. (42).

To analyze this behavior in more detail, the phase sensitivity is shown as a function of the input power in Fig. 7 with coherent input of Eq. (39), squeezed light mixed with coherent light of Eq. (40), and the SNL of Eq. (42) for comparison. As expected, it can be seen that the phase sensitivity for a coherent input improves with increasing power by the same scaling as the SNL. Even with a higher loss and thus a lower η, the scaling is similar and just the performance decreases slightly by a factor of $1/\sqrt{\eta}$. In case of using squeezed light,
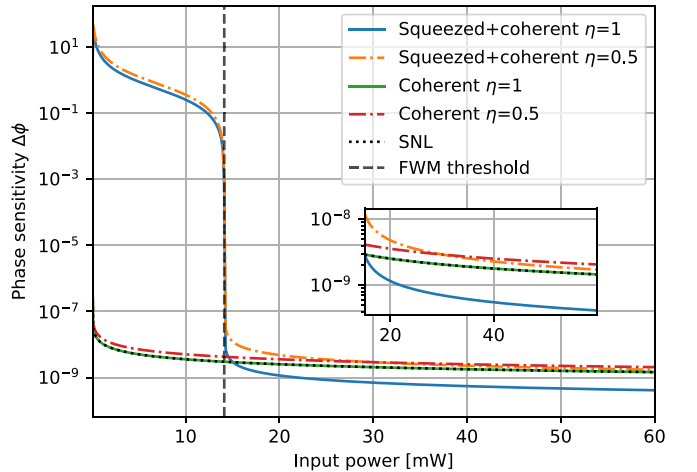

FIG. 7. Phase sensitivity over the input power for squeezed light mixed with coherent light [blue (solid dark) lossless and orange (dash-dotted light gray) with losses], coherent light [green (solid behind black dots) lossless and red (dash-dotted dark gray) with losses], and the SNL (black dotted). The FWM threshold is shown in black dashed line. For the calculation, the following values are used: $\Delta_i = \Delta_s = \Delta_p = 0$, $X = 0.01$, $n_{\text{eff}} = 1.801$, $n_g = 2.100\,87$, $\alpha_{\text{loss}} = 0.23$ m^{-1}, $L = 2\pi \times 220 \times 10^{-6}$ m, $\lambda_p = 1550 \times 10^{-6}$ m, $n_2 = 2.4 \times 10^{-19}$ m^2/W, $A_{\text{eff}} = 1.055\,64 \times 10^{-12}$ m^2.

P_l is increased close to threshold with $\sigma_n = 0.99895$ which corresponds to a power of $P_l = 14.12$ mW, while $P_c = 0$. Note that P_l does not contribute to the sensor performance but to the SNL as indicated by Eq. (42). Instead, P_l is required to pump the ring resonator and generates only a weak two-mode squeezed light that is available for sensing. The generated signal and idler power at $\sigma_n = 0.99895$ is $P_s = P_i \approx 1.13 \times 10^{-10}$ mW, which is very low compared to the input power. With increasing power and thus a larger σ_n, the sensitivity $\Delta\phi_s$ increases. However, the performance by using coherent light is still much better than using squeezed light, which can achieve a phase sensitivity of about 0.008. By keeping P_l constant at 14.12 mW close to the threshold and increasing P_c, the performance is improved significantly and the phase sensitivity of the squeezed light mixed with coherent light surpasses the coherent as well as the SNL performance. This is possible just due to the small amount of squeezed light.

However, the impact of losses on squeezed light is much larger than on coherent light, which is in agreement with [32]. Despite this fact, the scaling over input power is still better for the lossy case of the squeezed light mixed with coherent light and thus it surpasses the lossy coherent performance and would also improve further compared to the SNL. This is shown in the zoomed part of Fig. 7.

In order to achieve useful quantum enhancement and an advantage over the exclusive use of classical light, two essential requirements must be met. The first one is that a low threshold power needs to be achieved, because the scaling of the squeezed light mixed with coherent light is superior to using only coherent light. However, this advantage only applies if the threshold allows the squeezed light sensitivity to surpass the coherent sensitivity at a reasonable power. The threshold can be changed by adapting the design, as shown in Eq. (21), or by using a material with a high-nonlinear susceptibility. The second requirement is that the losses inside of the sensor region need to be below a critical value. In chip-integrated optical sensors, these losses depend mostly on the scale of the sensor region with Eq. (B4). A smaller sensor region may correspond to lower losses, but also a weaker signal since the light requires a certain interaction length with the stimulus. Examples for this are Sagnac interferometers in which a larger sensing area leads to a stronger phase shift or Raman measurements, in which the interaction length between the light and the molecules enhances the signal. To analyze the performance improvement of squeezed light compared to coherent light, we define the improvement factor $\mathbb{I}$ which is the ratio between $\Delta\phi_c$ and $\Delta\phi_s$ with

$$\mathbb{I} = \frac{\Delta\phi_c}{\Delta\phi_s}. \qquad (43)$$

Since the squeezing depends on the decay rates κ and γ as it is shown in Fig. 6, Eq. (43) is analyzed for a variation of the ratio of both which we define as the decay ratio with

$$\text{DR} = \frac{\kappa}{\gamma}. \qquad (44)$$

The results of Eq. (43) are shown in Fig. 8 over the length of the sensor region L as well as the efficiency η. It can be seen that for short lengths and rising decay ratios the improvement factor rises as well, which proves the quantum advantage. The
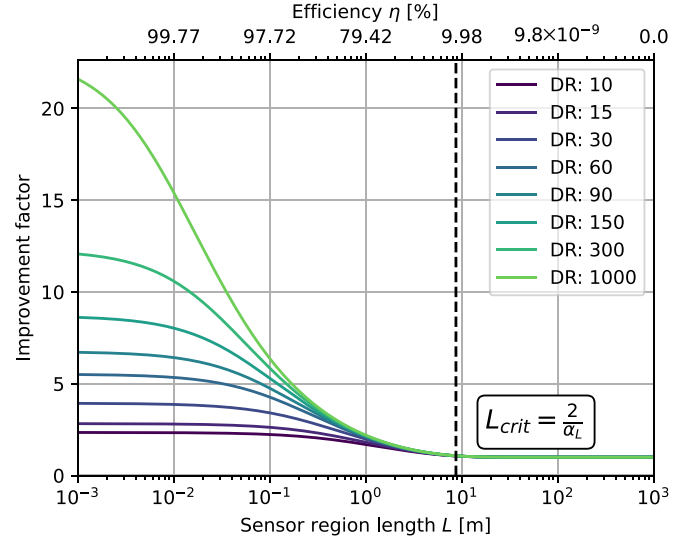

FIG. 8. Improvement factor evaluated with Eq. (43) over the waveguide length of the sensor region for different decay ratios from dark to light for a rising decay ratio. For the calculation, the following values are used: $\Delta_i = \Delta_s = \Delta_p = 0$, $X = 0.01$, $n_{\text{eff}} = 1.801$, $n_g = 2.10087$, $\alpha_{\text{loss}} = 0.23$ m^{-1}, $L = 2\pi \times 220 \times 10^{-6}$ m, $\lambda_p = 1550 \times 10^{-6}$ m, $n_2 = 2.4 \times 10^{-19}$ m^2/W, $A_{\text{eff}} = 1.05564 \times 10^{-12}$ m^2.

improvement factor for a short length and a high η can be approximated with

$$\mathbb{I}_{\text{Length}\to 0} = 10.218\ln(\text{DR} + 143.47) - 49.816. \qquad (45)$$

In contrast to this is the behavior with long lengths where $\mathbb{I}$ reaches 1. This can be explained by the fact that losses increase with length and the squeezed state is highly susceptible to them. After a certain length most of the squeezing is lost and no advantage can be achieved. We call this length the critical length which depends on the losses and can be approximated as

$$L_{\text{crit}} = \frac{2}{\alpha_{\text{loss}}} \qquad (46)$$

which corresponds to an efficiency $\eta \approx 13.5\%$. For a useful improvement factor of more than 1.5, the efficiency needs to be above 60%. This behavior confirms our starting motivation, that the quantum enhancement shows its strength for chip-integrated applications which mostly consist of short lengths and low-loss applications. Dependent on the use case, it can be useful to decrease the size of a sensor and to increase the sensitivity using two-mode squeezed light.

VIII. CONCLUSION

In this paper we analyzed the generation of two-mode squeezed light in a ring-resonator cavity and its application for sensing a phase shift in an MZI. The results show that the combination of squeezed and coherent light in a low-loss sensor region can improve the sensitivity compared to the SNL and a classical sensing system. We started with a linearized Hamiltonian for the FWM process and derived the expectation values of the outracavity signal and idler modes via the input-output theory. They are used to determine the

squeezing behavior of the two-mode squeezed light and to give a support to design a cavity for the desired squeezing behavior. Additionally, the derived equations are used to calculate the minimum detectable phase change inside of an MZI and it has been shown that squeezed light mixed with coherent light can surpass the phase sensitivity of the SNL. Thus, equations are derived which describe the performance of the whole system consisting of a ring resonator for the squeezed light generation in addition with the MZI and ID detection.

However, it is important for a real use case to tune the threshold by design and material choice in a reasonable region, where the improved slope of the squeezed light can show its full potential. Furthermore, we showed that the losses of a system limit the usability of two-mode squeezed light. The reason is that squeezed light is very loss sensitive and after a certain length of the sensor region most of the squeezing is lost and no improvement can be achieved compared to a classical sensor. However, if the sensor region is small and has low losses, two-mode squeezed light can significantly increase the performance by more than a factor of 10. It was shown that this improvement factor depends on the decay ratio and thus on the design of the cavity. This leads to an optimization problem between a desired decay ratio and a low threshold. If both are reasonably chosen, the quantum enhancement can be beneficial.

In summary we think that this can lead to more compact sized optical sensors which can have the same sensitivity at a small size as with a larger sensor region due to the quantum enhancement. It is important to note that squeezed light can improve the performance of many various optical sensor concepts and, as shown in this paper, especially for interferometer based sensor principles that are nowadays already available to manufacture and to use.

APPENDIX A: GAIN OF THE FOUR-WAVE MIXING PROCESS

Based on the derivation in [11] the gain of the FWM process inside of a ring resonator can be given in the following expression:

$$g = \frac{\hbar \left(\omega_p^2 \omega_s \omega_i \right)^{1/4} v_g^2 \gamma_{\mathrm{NL}}}{L} \tag{A1}$$

with the group velocity v_g, the length of the resonator L, and the nonlinear waveguide parameter γ_{NL} which is given by [33]

$$\gamma_{\mathrm{NL}} = \frac{\omega_p n_2}{c A_{\mathrm{eff}}} \tag{A2}$$

with the effective mode area of the optical waveguide mode A_{eff} and the nonlinear refractive index n_2 which can be described as

$$n_2 = \frac{3 \chi^{(3)}}{4 \varepsilon_0 c n_{\mathrm{eff}}^2} \tag{A3}$$

and the effective refractive index n_{eff}. Since n_2 is mostly used in the literature we give our final gain as follows:

$$g = \frac{\hbar \omega_p \left(\omega_p^2 \omega_s \omega_i \right)^{1/4} v_g^2 n_2}{c A_{\mathrm{eff}} L} \approx \frac{\hbar \omega_p^2 v_g^2 n_2}{c A_{\mathrm{eff}} L}. \tag{A4}$$

Note that the derivations slightly differ from each other as in [34]. Since it is derived with some approximations, the gain can only be confirmed by experiments.

APPENDIX B: PHYSICAL RELATION TO THE PARAMETERS

For a practical realization of a system it is very important to know the physical relation of the operators and how they depend on the structure dimensions. The parameters for the design of the ring resonator are the decay rate γ and the coupling rate κ. They describe how much light decays via the respective effect at each round-trip time which is described as follows for a laser pulse:

$$t_{\mathrm{round}} = \frac{n_{\mathrm{eff}} L}{c} \tag{B1}$$

with the effective refractive index of the waveguide n_{eff}, the length of the ring L, and the speed of light c. At each round trip a certain part of the light couples out of the ring resonator into the connected waveguide by a certain fraction and this is described by the cross coupling X which takes the values $0 \leqslant X \leqslant 1$. All the light is coupled to the waveguide at a value of 1 and no light at a value of zero. Thus, the coupling rate can be defined as the light that is coupled out per round trip:

$$\kappa = \frac{X}{t_{\mathrm{round}}} = \frac{Xc}{n_{\mathrm{eff}} L}. \tag{B2}$$

Additionally, at each round trip a certain part of the light is scattered away caused by for example scattering on rough waveguide walls. In general, the optical power P in lossy photonic chip-integrated waveguides over a length L can be described by the following equation [35]:

$$P(L) = P_0 e^{-\alpha_{\mathrm{loss}} L} \tag{B3}$$

with the optical waveguide losses α_{loss} in the units of m^{-1}. To model the losses now in dependency of the waveguide losses and together with the knowledge that $P(L) \leqslant P_0$, we simply define it as the relative power change with a value of 1 for no losses and a value of zero for maximum losses:

$$\eta = 1 - \frac{P_0 - P(L)}{P_0} = e^{-\alpha_{\mathrm{loss}} L}. \tag{B4}$$

Based on this we can define the decay rate per round trip time as follows:

$$\gamma = \frac{1 - \eta}{t_{\text{round}}} = \frac{(1 - e^{-\alpha_{\text{loss}}L})c}{n_{\text{eff}}L}. \tag{B5}$$

Another important physical parameter is the complex amplitude of a coherent pump. It is known that this can be described as

$$\alpha_l = \sqrt{\frac{P}{\hbar\omega_p}} \exp(i\phi_l) \tag{B6}$$

with the pump power P and the frequency of the light ω_p and is proportional to a photon flux. Note that α_l has the unit of $\sqrt{\text{Hz}}$. However, the intracavity amplitude of Eq. (7) α_p in the main text is unitless and cannot be converted back to the optical power using Eq. (B6). To achieve this, it is necessary to transfer the units to hertz which is done with defining the transmission rate with

$$t = \frac{(1 - X)c}{n_{\text{eff}}L}. \tag{B7}$$

This is just the counterpart of the coupling rate and defines the rate of photons staying either in the resonator or in the straight waveguide. The intracavity amplitude in units of hertz can then be derived as $a_{p,\sqrt{\text{Hz}}} = \sqrt{t}a_p$.

Another important parameter for the FWM process is the injection parameter σ and its relation to the FWM threshold. The physical dependency for the injection parameter can be given as

$$\sigma = \frac{2g\kappa}{(\Gamma/2 - i\Delta)^2} \frac{P_l}{\hbar\omega_p}. \tag{B8}$$

It is possible to derive the FWM threshold power that is required in the waveguide P_l in Fig. 2 by using the relation $\sigma_{\text{th}} = \Gamma$ and Eq. (B6). This leads to

$$P_{\text{th}} = \frac{\Gamma\hbar\omega_p(\Gamma/2 - i\Delta_p)^2}{2g\kappa} \overset{\Delta=0}{=} \frac{\Gamma^3\hbar\omega_p}{8g\kappa}. \tag{B9}$$

Note that effects like self-phase and cross-phase modulation are neglected in Eq. (B9) and thus the real P_{th} might be higher.

APPENDIX C: QUADRATURE MEASUREMENT

In the following, the determination of the quadrature measurement shown in Fig. 4 is explained in more detail. One input of the BS consists of the generated signal and idler $a_{\text{BS},1} = a_s \exp(-i[\omega_s t + \phi_s]) + a_i \exp(-i[\omega_i t + \phi_i])$ with a certain phase ϕ_s and ϕ_i for the signal and idler. The other input consists of a local oscillator with a strong coherent background that includes waves of the signal and idler frequency with $a_{\text{BS},2} = |\alpha_{\text{LO}}|\{\exp(-i[\omega_s t + \phi_{\text{LO}}]) + \exp(-i[\omega_i t + \phi_{\text{LO}}])\}$ and the phase ϕ_{LO}. In the following, we assume that the signal and idler phases match with $\phi_i = \phi_s$. Both inputs are mixed at the beam splitter with the matrix from Eq. (32), detected, and the measured signal is subtracted which leads to

$$X_Q = d_1^\dagger d_1 - d_2^\dagger d_2$$
$$= |\alpha_{\text{LO}}|(a_s e^{-i(\delta_{\text{LO}} + t[\omega_s - \omega_i])} + a_s^\dagger e^{i(\delta_{\text{LO}} + t[\omega_s - \omega_i])})$$

$$+ |\alpha_{\text{LO}}|(a_i e^{i(-\delta_{\text{LO}} + t[\omega_s - \omega_i])} + a_i^\dagger e^{-i(-\delta_{\text{LO}} + t[\omega_s - \omega_i])})$$
$$+ |\alpha_{\text{LO}}|([a_i + a_s]e^{-i\delta_{\text{LO}}} + [a_i^\dagger + a_s^\dagger]e^{i\delta_{\text{LO}}}) \tag{C1}$$

with the difference between the signal, idler, and the LO phase $\delta_{\text{LO}} = \phi_i - \phi_{\text{LO}}$. Equation (C1) includes one fast oscillating and one static term. Since the fast oscillating one cannot be measured by a physical detector, the static one is measured which corresponds to the quadrature signal of Eq. (27). Note that the local oscillator is required in this measurement scheme. The reason is that squeezed light consists generally only of a low amount of photons. Using a local oscillator with a strong coherent background amplifies the quadrature information of the squeezed light to make it measurable.

APPENDIX D: OUTRACAVITY EXPECTATION VALUES

In the following, the results of the calculated outracavity expectation values are given and determined based on Eq. (19). To keep the results general, we determine the expectation values for the case that the signal and idler inputs are in the vacuum state and for the other case that they are in a coherent state with $b_{\text{in},s} = \alpha_s$ and $b_{\text{in},i} = \alpha_i$. Therefore, the expectation values are split into a static $\langle b_{\text{st}}\rangle$ and a fluctuating part $\langle b_f\rangle$ with the total expectation value being $\langle b_{\text{out}}\rangle = \langle b_f\rangle + \langle b_{\text{st}}\rangle$. If a vacuum input is assumed then only the fluctuation results are of interest as it is done in the main text. Otherwise, for a coherent input, $\langle b_f\rangle$ and $\langle b_{\text{st}}\rangle$ need to be added. However, only the signal modes and some cross products between the signal and idler modes are given. The reason is that due to the symmetry in FWM the idler results can be simply achieved by a replacement of the index in the equations. Based on them, all desired expectation values can be determined.

1. Fluctuating results

For the fluctuating results with $\alpha_{i/s} = 0$, all first-order expectation values are zero, $\langle b_{s,f}(\omega)\rangle = \langle b_{s,f}^\dagger(\omega)\rangle = 0$, and we have the following second-order values: $\langle b_{s,f}(\omega)b_{s,f}(\omega')\rangle = \langle b_{s,f}^\dagger(\omega)b_{s,f}^\dagger(\omega')\rangle = \langle b_{i,f}(\omega)b_{s,f}^\dagger(\omega')\rangle = \langle b_{s,f}(\omega)b_{i,f}^\dagger(\omega')\rangle = \langle b_{s,f}^\dagger(\omega)b_{i,f}(\omega')\rangle = \langle b_{i,f}^\dagger(\omega)b_{s,f}(\omega')\rangle = 0.$ The relevant
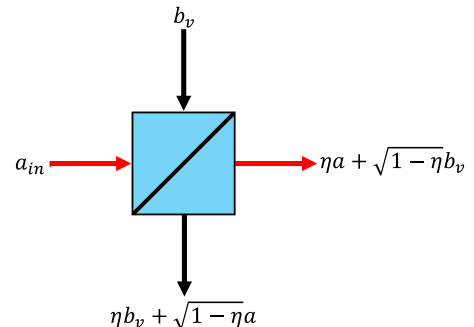

FIG. 9. Schematic of a BS that models the losses.

results are given in the following:

$$\langle b_{i,f}(\omega)b_{s,f}(\omega')\rangle = \frac{-2\kappa\sigma[4\Delta_i\Delta_s - 2i\Gamma(\Delta_i + \Delta_s) - \Gamma^2 - \sigma^2]}{\Xi - 2\sigma^2\Gamma^2}\delta(\omega - \omega'), \tag{D1}$$

$$\langle b_{i,f}^\dagger(\omega)b_{s,f}^\dagger(\omega')\rangle = \frac{-2\kappa\sigma[4\Delta_i\Delta_s + 2i\Gamma(\Delta_i + \Delta_s) - \Gamma^2 - \sigma^2]}{\Xi - 2\sigma^2\Gamma^2}\delta(\omega - \omega'). \tag{D2}$$

The equation for the photon number $\langle b_{s,f}^\dagger(\omega)b_{s,f}(\omega')\rangle$ is already given in Eq. (21). Note that the other expectation values can be determined either due to the relation $\langle b_{s,f}(\omega)b_{s,f}^\dagger(\omega')\rangle = 1 + \langle b_{s,f}^\dagger(\omega)b_{s,f}(\omega')\rangle$ or due to symmetries like $\langle b_{i,f}^\dagger(\omega)b_{s,f}^\dagger(\omega')\rangle = \langle b_{s,f}^\dagger(\omega)b_{i,f}^\dagger(\omega')\rangle$. Thus, all expectation values for the fluctuating results can be determined with the few given equations.

2. Static results

For the static results each expectation value is not equal to zero. However, to determine each expectation value only the following two equations (D3) and (D4) are required and the rest can be determined using symmetries:

$$\langle b_{s,st}(\omega)\rangle = \frac{\alpha_s\{\kappa^2 + \sigma^2 - \gamma^2 - 4\Delta_i\Delta_s - 2i[\Delta_i(\gamma - \kappa) + \Delta_s\Gamma]\} - 2\alpha_i\kappa\sigma}{4\Delta_i\Delta_s + 2i\Gamma(\Delta_i - \Delta_s) + \Gamma^2 - \sigma^2}, \tag{D3}$$

$$\langle b_{s,st}^\dagger(\omega)\rangle = \frac{\alpha_s\{\kappa^2 + \sigma^2 - \gamma^2 - 4\Delta_i\Delta_s + 2i[\Delta_i(\gamma - \kappa) + \Delta_s\Gamma]\} - 2\alpha_i\kappa\sigma}{4\Delta_i\Delta_s - 2i\Gamma(\Delta_i - \Delta_s) + \Gamma^2 - \sigma^2}. \tag{D4}$$

The other equations can be simply determined by a factorization with

$$\langle b_{s,st}(\omega)b_{s,st}^\dagger(\omega')\rangle = \langle b_{s,st}(\omega)\rangle\langle b_{s,st}^\dagger(\omega')\rangle, \tag{D5}$$

$$\langle b_{s,st}^\dagger(\omega)b_{s,st}(\omega')\rangle = \langle b_{s,st}^\dagger(\omega)\rangle\langle b_{s,st}(\omega')\rangle, \tag{D6}$$

$$\langle b_{i,st}(\omega)b_{s,st}(\omega')\rangle = \langle b_{i,st}(\omega)\rangle\langle b_{s,st}(\omega')\rangle, \tag{D7}$$

or by changing the index between the signal and idler modes. In this way, all static expectation values can be determined.

APPENDIX E: WAVEGUIDE LOSSES IN THE MZI

Losses in quantum systems are mostly modeled using a BS description with an efficiency η as follows:

$$\mathbf{LM} = \begin{pmatrix} \sqrt{\eta} & \sqrt{1-\eta} \\ \sqrt{1-\eta} & -\sqrt{\eta} \end{pmatrix}. \tag{E1}$$

Thereby, η is in the range $0 \leqslant \eta \leqslant 1$ with a value of $\eta = 1$ for no losses and is described by Eq. (B4). It is important to note that while a part of a waveguide mode a_{in} is lost, vacuum is coupled into the system [29]. This is shown in Fig. 9 and the resulting mode can be determined by

$$a_{\text{out}} = \sqrt{\eta}a_{\text{in}} + \sqrt{1-\eta}b_v \tag{E2}$$

and the vacuum bath mode b_v. The part that couples out of the waveguide can be described by (E1). The second output of our virtual BS is ignored.
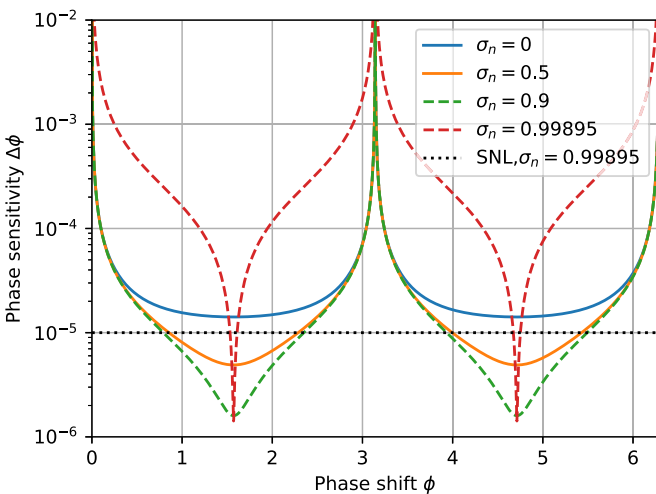
FIG. 10. Phase sensitivity over the MZI phase shift ϕ with a weak coherent pump $\alpha_c = 10^5\sqrt{\text{Hz}}$ and for different σ_n.
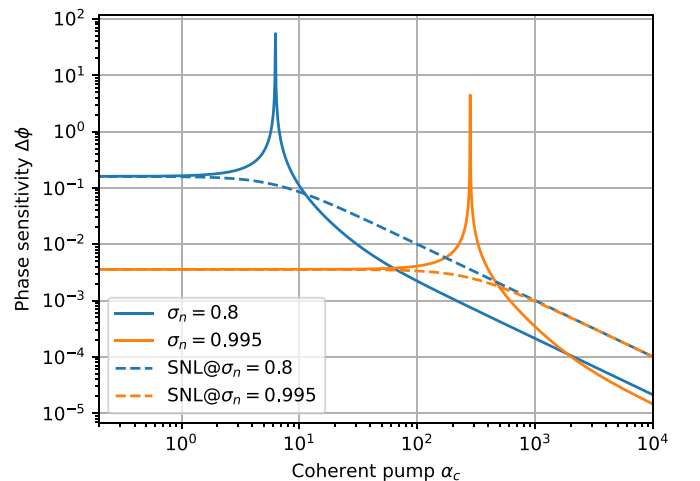
FIG. 11. Phase sensitivity over the coherent pump α_c at MZI phase shift $\phi = \pi/2$ for different σ_n.

APPENDIX F: MZI PHASE SENSITIVITY

In the following, the phase sensitivity for the MZI in Fig. 1 and Eq. (36) is discussed in more detail. The behavior over the phase shift inside of the MZI is analyzed first and shown in Fig. 10 for a weak coherent signal $\alpha_c = 10^5$ and for different pump power σ_n. It can be seen that the sensitivity diverges for a phase of $\phi = 0$ and $\pi/2$ while it reaches the optimum at $\phi = \frac{\pi}{2}$ and $\frac{3\pi}{2}$ which should be the preferred working points for a sensing application that can surpass the SNL. Additionally, the sensitivity increases together with σ_n. This is clear since the squeezing increases as well with σ_n. In comparison, also the SNL using Eq. (42) with $\alpha_p = 0\sqrt{\text{Hz}}$ is shown for the case with the $\sigma_n = 0.998\,95$. As expected, the phase sensitivity for the same pump surpasses the SNL by more than a magnitude. This shows that two-mode squeezed light can be used for quantum-enhanced metrology, which matches other work [36].

Additionally, it is interesting to analyze the pole point that results out of Eq. (40). Therefore, Eq. (40) is plotted over the coherent pump α_c for two different σ_n values in Fig. 11. It can be seen that for both σ_n values a pole is visible which is similar to the results of other works [37]. Interestingly, the position of this pole point appears if the number of photons of the coherent pump $|\alpha_c|^2$ matches the number of photons of the squeezed states $\langle a_s^\dagger a_s \rangle + \langle a_i^\dagger a_i \rangle$. The phase sensitivity of the MZI is constant up to the pole position and improves afterwards with rising α_c. For both σ_n values, the improvement is similar after the pole while the curve using the higher σ_n surpasses the lower one. However, before the pole point, the phase sensitivity is the same as the SNL. This matches the results of [38] and shows that a high coherent pump is required to achieve an improved scaling compared to the SNL.

[1] W. Nawrocki, *Introduction to Quantum Metrology* (Springer, New York, 2019).

[2] V. Giovannetti, S. Lloyd, and L. Maccone, Quantum metrology, Phys. Rev. Lett. **96**, 010401 (2006).

[3] V. Giovannetti, S. Lloyd, and L. Maccone, Advances in quantum metrology, Nat. Photonics **5**, 222 (2011).

[4] U. Dorner, R. Demkowicz-Dobrzanski, B. J. Smith, J. S. Lundeen, W. Wasilewski, K. Banaszek, and I. A. Walmsley, Optimal quantum phase estimation, Phys. Rev. Lett. **102**, 040403 (2009).

[5] R. Demkowicz-Dobrzański, M. Jarzyna, and J. Kołodyński, Quantum limits in optical interferometry, in *Progress in Optics*, edited by E. Wolf (Elsevier, Amsterdam, 2015), Vol. 60, Chap. 4, pp. 345–435.

[6] B. P. Abbott *et al.* (LIGO Scientific Collaboration and Virgo Collaboration), Observation of gravitational waves from a binary black hole merger, Phys. Rev. Lett. **116**, 061102 (2016).

[7] H. Vahlbruch, A. Khalaidovski, N. Lastzka, C. Gräf, K. Danzmann, and R. Schnabel, The GEO 600 squeezed light source, Class. Quantum Grav. **27**, 084027 (2010).

[8] L. Chang, W. Xie, H. Shu, Q.-F. Yang, B. Shen, A. Boes, J. D. Peters, W. Jin, C. Xiang, S. Liu, G. Moille, S.-P. Yu, X. Wang, K. Srinivasan, S. B. Papp, K. Vahala, and J. E. Bowers, Ultra-efficient frequency comb generation in AlGaAs-on-insulator microresonators, Nat. Commun. **11**, 1331 (2020).

[9] T. Fortier and E. Baumann, 20 years of developments in optical frequency comb technology and applications, Commun. Phys. **2**, 153 (2019).

[10] J. M. Arrazola *et al.*, Quantum circuits with many photons on a programmable nanophotonic chip, Nature (London) **591**, 54 (2021).

[11] Z. Vernon and J. E. Sipe, Strongly driven nonlinear quantum optics in microring resonators, Phys. Rev. A **92**, 033840 (2015).

[12] S. Fujii and T. Tanabe, Dispersion engineering and measurement of whispering gallery mode microresonator for Kerr frequency comb generation, Nanophotonics **9**, 1087 (2020).

[13] J. Heebner, R. Grover, and T. Ibrahim, *Optical Microresonators: Theory, Fabrication, and Applications*, Springer Series in Optical Sciences, Vol. 138 (Springer, New York, 2008), pp. 71–103.

[14] M. J. Collett and C. W. Gardiner, Squeezing of intracavity and traveling-wave light fields produced in parametric amplification, Phys. Rev. A **30**, 1386 (1984).

[15] C. W. Gardiner and M. J. Collett, Input and output in damped quantum systems: Quantum stochastic differential equations and the master equation, Phys. Rev. A **31**, 3761 (1985).

[16] M. O. Scully and M. S. Zubairy, *Quantum Optics* (Cambridge University, New York, 1997).

[17] P. Lambropoulos and D. Petrosyan, System-reservoir interaction, *Fundamentals of Quantum Optics and Quantum Information* (Springer-Verlag, Berlin, Heidelberg, 2007), pp. 119–149.

[18] P. Zoller and C. W. Gardiner, Quantum noise in quantum optics: The stochastic Schrödinger equation, arXiv:quant-ph/9702030.

[19] H. M. Wiseman and G. J. Milburn, *Quantum Measurement and Control* (Cambridge University, New York, 2009).

[20] C. Navarrete-Benlloch, E. Roldán, Y. Chang, and T. Shi, Regularized linearization for quantum nonlinear optical cavities: application to degenerate optical parametric oscillators, Opt. Express **22**, 24010 (2014).

[21] P. Degenfeld-Schonburg, C. Navarrete-Benlloch, and M. J. Hartmann, Self-consistent projection operator theory in nonlinear quantum optical systems: A case study on degenerate optical parametric oscillators, Phys. Rev. A **91**, 053850 (2015).

[22] P. Degenfeld-Schonburg, M. Abdi, M. J. Hartmann, and C. Navarrete-Benlloch, Degenerate optomechanical parametric oscillators: Cooling in the vicinity of a critical point, Phys. Rev. A **93**, 023819 (2016).

[23] V. D. Vaidya, B. Morrison, L. G. Helt, R. Shahrokshahi, D. H. Mahler, M. J. Collins, K. Tan, J. Lavoie, A. Repingon, M. Menotti, N. Quesada, R. C. Pooser, A. E. Lita, T. Gerrits, S. W. Nam, and Z. Vernon, Broadband quadrature-squeezed vacuum and nonclassical photon number correlations from a nanophotonic device, Sci. Adv. **6**, eaba9186 (2020).

[24] K. Ikeda, R. E. Saperstein, N. Alic, and Y. Fainman, Thermal and Kerr nonlinear properties of plasma-deposited silicon

nitride/silicon dioxide waveguides, Opt. Express **16**, 12987 (2008).

[25] K. Zielnicki, K. Garay-Palmett, D. Cruz-Delgado, H. Cruz-Ramirez, M. F. O'Boyle, B. Fang, V. O. Lorenz, A. B. U'Ren, and P. G. Kwiat, Joint spectral characterization of photon-pair sources, J. Mod. Opt. **65**, 1141 (2018).

[26] D. Walls and G. J. Milburn, Quantisation of the electromagnetic field, in *Quantum Optics*, edited by D. Walls and G. J. Milburn (Springer-Verlag, Berlin, 2008), pp. 7–27.

[27] Y. K. Chembo, Quantum dynamics of Kerr optical frequency combs below and above threshold: Spontaneous four-wave mixing, entanglement, and squeezed states of light, Phys. Rev. A **93**, 033820 (2016).

[28] C. Gerry and P. Knight, *Introductory Quantum Optics* (Cambridge University, New York, 2004).

[29] H.-A. Bachor and T. C. Ralph, Appendices, in *A Guide to Experiments in Quantum Optics* (Wiley, New York, 2004), pp. 407–415.

[30] S. L. Braunstein and C. M. Caves, Statistical distance and the geometry of quantum states, Phys. Rev. Lett. **72**, 3439 (1994).

[31] R. Kubo, Generalized cumulant expansion method, J. Phys. Soc. Jpn. **17**, 1100 (1962).

[32] R. Schnabel, Squeezed states of light and their applications in laser interferometers, Phys. Rep. **684**, 1 (2017).

[33] G. Agrawal, Pulse propagation in fibers, in *Nonlinear Fiber Optics*, 5th ed., edited by G. Agrawal (Academic, New York, 2013), Chap. 2, pp. 27–56.

[34] U. B. Hoff, B. M. Nielsen, and U. L. Andersen, Integrated source of broadband quadrature squeezed light, Opt. Express **23**, 12013 (2015).

[35] R. G. Hunsperger, Losses in optical waveguides, in *Integrated Optics: Theory and Technology* (Springer-Verlag, Berlin, 2002), pp. 93–111.

[36] O. Steuernagel and S. Scheel, Approaching the Heisenberg limit with two-mode squeezed states, J. Opt. B **6**, S66 (2004).

[37] S. Ataman, Optimal Mach-Zehnder phase sensitivity with Gaussian states, Phys. Rev. A **100**, 063821 (2019).

[38] L. Pezzé and A. Smerzi, Mach-Zehnder interferometry at the Heisenberg limit with coherent and squeezed-vacuum light, Phys. Rev. Lett. **100**, 073601 (2008).